EES Catalysis

PAPER

View Article Online
View Journal | View Issue

Cite this: *EES Catal.*, 2026, 4, 108

Solid-phase production of Co–N–C electrocatalysts at a kilogram scale *via* the Kirkendall effect for proton exchange membrane fuel cells

Jiaheng Huo,[ab] Wulyu Jiang,[c] Lu Xia,[c] Bruna Ferreira Gomes,[d] Yunxing Zhao,[e] Yinping Wei,[f] Xuya Zhu,[f] Dongsheng Xia,*[ab] Min Chen *[ab] and Lin Gan *[f]

Platinum-group metal-free single-atom catalysts (SACs) are vital for cost-effective fuel cells, yet their adoption is hindered by performance limitations and challenges in scalable production. While Fe–N–C SACs offer high activity, their stability is severely compromised by Fenton-induced degradation. To address this, Co–N–C SACs have emerged as promising alternatives due to their much lower Fenton activity and hence improved durability. However, conventional synthesis relies on solvent-intensive methods, limiting large-scale, environmentally friendly production and precise structural control. Here, we report a solid-phase synthesis strategy *via* the Kirkendall effect for the kilogram-scale production of Co-doped zeolitic imidazolate framework-8 (Co-ZIF-8) with high reproducibility and precise compositional control. Further pyrolysis at high temperatures enables the formation of structurally well-defined Co–N–C SACs with tunable composition, high site density, and superior scalability. The optimized catalyst, when integrated as the cathode in a representative proton exchange membrane fuel cell (PEMFC) system, delivers remarkable power densities of 0.70 W cm^{-2} and 0.39 W cm^{-2} in O_2 and air conditions, respectively, outperforming most reported Co-based catalysts. This work establishes a generalizable and environmentally sustainable route for the large-scale production of high-performance non-precious metal electrocatalysts, advancing PEMFC technology and broader electrochemical energy applications.

Received 30th August 2025,
Accepted 17th September 2025

DOI: 10.1039/d5ey00264h

rsc.li/eescatalysis

Broader context

Transition metal-doped zeolitic imidazolate framework-8 (TM-ZIF-8) represents a class of highly promising precursors for the preparation of high-performance TM–N–C single-atom catalysts (SACs), which show great potential in electrochemical applications such as proton exchange membrane fuel cells (PEMFCs). For the cathodic oxygen reduction reaction (ORR) in PEMFCs, Co-ZIF-8-derived Co–N–C SACs have demonstrated excellent ORR activity with improved operation stability compared to Fe–N–C, which makes them another highly competitive alternative to commercial platinum-based catalysts. However, conventional synthesis routes for Co-ZIF-8-derived Co–N–C SACs are highly organic solvent-intensive, which has largely impeded their scalable, controllable and reproducible production and thus achieving leapfrogging transition from lab-scale to industrialization. This work reports a solid-phase strategy for synthesizing Co-ZIF-8 precursors at a kilogram scale *via* the Kirkendall effect, enabling scalable production of high-performance Co–N–C SACs with both high controllability and excellent reproducibility. The novel strategy proposed in this work is believed to pave the way for the scalable production of other TM–N–C SACs for broader electrochemical energy applications.

[a] *School of Materials and Energy, Foshan University, Foshan, 528000, P. R. China. E-mail: dsxia@fosu.edu.cn*
[b] *Guangdong Provincial Key Laboratory of Green Energy Materials and Devices, Yunfu Industrial Technology Research Institute of New Energy and New Materials, Yunfu 527300, P. R. China. E-mail: minchen1981@126.com*
[c] *Faculty of Mechanical Engineering, RWTH Aachen University, Aachen, 52056, Germany*
[d] *Electrochemical Process Engineering, University of Bayreuth, Universitätstraße 30, Bayreuth, 95447, Germany*
[e] *Guangzhou Institute of Energy Conversion, Chinese Academy of Sciences (CAS), Guangzhou, 510640, P. R. China*
[f] *Key Laboratory of Electrocatalytic Materials and Green Hydrogen Technology of Guangdong Higher Education Institutes, Shenzhen Key Laboratory of Advanced Layered Materials for Value-added Applications, Institute of Materials Research, Tsinghua Shenzhen International Graduate School, Tsinghua University, Shenzhen, 518055, P. R. China. E-mail: lgan@sz.tsinghua.edu.cn*

Introduction

Proton exchange membrane fuel cells (PEMFCs) rely on efficient oxygen reduction reaction (ORR) catalysts to drive clean and sustainable energy conversion. However, their widespread deployment is severely constrained by the high cost and scarcity of platinum-group metal (PGM) catalysts, which currently dominate ORR performance.[1] To address this limitation, PGM-free single-atom catalysts (SACs) have emerged as promising alternatives, leveraging earth-abundant elements to reduce costs while maintaining catalytic efficiency.[2] Among PGM-free SACs, Fe–N–C catalysts exhibit the highest ORR activity, making them strong contenders for replacing PGM catalysts.[3–7] However, their long-term stability remains a critical challenge due to Fenton-induced degradation, where $Fe–N_4$ active sites undergo oxidative attack by hydroxyl ($^{\bullet}OH$) and hydroperoxide ($HO_2^{\bullet}$) radicals, leading to Fe demetallation and carbon oxidation.[8–10]

To overcome these stability limitations, Co–N–C SACs have gained attention as a more durable alternative, as Co-based active sites exhibit higher resistance to Fenton-induced degradation and lower susceptibility to demetallation.[11,12] Unfortunately, Co–N–C catalysts generally suffer from lower intrinsic ORR activity and reduced four-electron selectivity, necessitating further optimization of active site density and electronic structure to bridge the performance gap with Fe–N–C.[13] A widely adopted strategy for synthesizing Co–N–C SACs is pyrolysis of Co-doped zeolitic imidazolate framework-8 (Co-ZIF-8), which yields catalysts with atomically dispersed $Co–N_4$ moieties and a well-defined porous carbon structure, enhancing active site accessibility.[14–16] Moreover, the ZIF-derived nitrogen–carbon framework has proven effective for anchoring active sites in various TM–N–C (TM = transition metal) catalysts, demonstrating its versatility in single-atom catalysis.[17–20]

However, the conventional synthesis of Co-ZIF-8 heavily relies on solvent-based methods, which require substantial amounts of organic solvents such as methanol and ethanol.[21,22] This raises environmental concerns, increases production complexity, and undermines the cost advantages of PGM-free catalysts. Furthermore, wet chemistry approaches introduce stringent process control requirements, making large-scale, reproducible production challenging. Therefore, developing a scalable, solvent-free synthesis strategy for Co-ZIF-8 is crucial to achieving large-scale production of Co–N–C SACs while maintaining precise compositional control. Recent efforts have explored solid-phase synthesis routes, eliminating solvents and simplifying processing steps. Lin *et al.* first introduced a solvent-free synthesis of ZIF-8 using solid-state reactions between 2-MIm and ZnO.[23] Inspired by this work, Zhao *et al.* successfully extended this approach to Fe-MOF precursors, demonstrating its feasibility for Fe–N–C catalysts.[24] Similarly, Liu *et al.* synthesized high-performance Fe–N–C SACs *via* solid-phase chemistry using ferrous oxalate as an Fe precursor.[25] Despite these advances, a scalable, green synthesis of Co–N–C SACs *via* solid-phase chemistry has yet to be reported. Furthermore, the underlying reaction mechanism at the solid reactant interfaces remains poorly understood, limiting further optimization and reproducibility.

In this work, we report a single-batch kilogram-scale synthesis of Co-ZIF-8 crystals *via* solid-phase reactions, where the Kirkendall effect induced by the unequal interdiffusion between TM oxide precursors and organic ligands was identified as the key mechanism for the reaction process. We demonstrate precise control over Co concentration (0–80%), enabling tunable synthesis of Co–N–C SACs. The optimized 3.3% Co-ZIF-8 precursor was pyrolyzed into a Co–N–C catalyst with exclusively single-atom $Co–N_4$ active sites, ensuring high catalytic site density and structural integrity. The optimized Co–N–C cathode in a single PEMFC achieves a remarkable power density of 0.70 W cm^{-2} and 0.39 W cm^{-2} under $H_2–O_2$ and H_2–air conditions, respectively. More importantly, highly consistent batch-to-batch ORR activities further demonstrate superior reproducibility of the proposed solid-phase strategy. This work establishes a generalizable and environmentally sustainable approach for large-scale production of high-performance TM–N–C single-atom catalysts, paving the way for the next generation of cost-effective PEMFC technology.

Results and discussion

Synthesis and structure of the Co-ZIF-8 precursor

We began by designing a solid-phase strategy for the scalable synthesis of Co-ZIF-8, aiming to address the limitations of conventional solvent-based precursor fabrication. Unlike wet-chemistry methods, our approach eliminates organic solvents while ensuring precise compositional control and kilogram-scale production in a single batch. To achieve controlled Co incorporation, we employed a direct solid-phase reaction between 2-MIm and ZnO/Co_3O_4 nanoparticles at 220 °C for 18 hours. The resulting Co-ZIF-8 precursors (*m*Co-ZIF-8, where *m*% denotes the Co molar fraction) exhibited porous and hollow morphology (Fig. 1a and Fig. S1). As the Co content increased, the precursor color gradually transitioned from lilac to dark purple and eventually to black (Fig. 1b), suggesting progressive Co incorporation into the ZIF-8 framework. Powder X-ray diffraction (XRD) (Fig. 1d) confirmed that, despite Co doping levels ranging from 0 to 80%, the ZIF-8 crystallinity remained intact, indicating successful atomic-level Co substitution within the lattice. Through ball milling, the particle size of the Co-ZIF-8 precursor can be reduced to ~50 nm (Fig. 1c), accompanied by a 2.7-fold increase in its external surface area from 40.2 to 110.0 $m^2 g^{-1}$ (Fig. S2 and Table S1). This is crucial for maximizing the active site density and accessibility of the subsequently prepared Co–N–C catalysts.[26]

To assess the scalability of our process, we systematically increased the reactant dosage and reactor capacity, achieving kilogram-scale synthesis of the 3.3Co-ZIF-8 precursors in a single batch (Fig. 1f). Notably, the crystallinity, morphology, and compositional homogeneity remain unchanged, confirming that our method maintains structural and chemical fidelity even at kilogram scales. This solid-phase strategy offers a

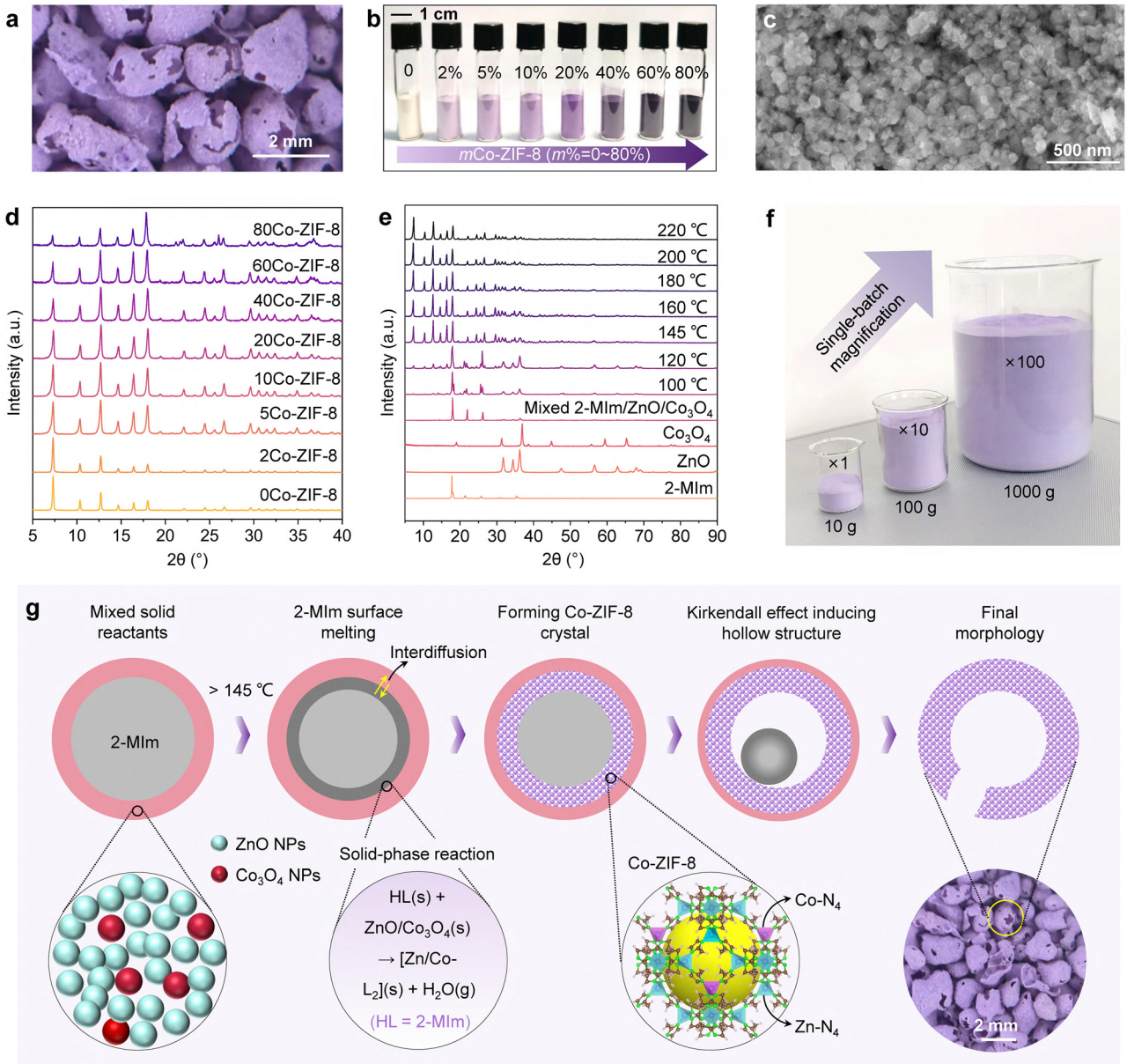

Fig. 1 (a) Digital photograph of the 3.3Co-ZIF-8 precursor particles, macroscopically showing loose and porous structure features. (b) Digital photos of the *m*Co-ZIF-8 precursor powders with various Co doping concentrations. (c) SEM image of the ball-milled 3.3Co-ZIF-8 precursor. (d) XRD patterns of the *m*Co-ZIF-8 series precursors. (e) XRD patterns of 2-MIm, ZnO, Co_3O_4, and their reaction products (3.3Co%) with different reaction temperatures (each temperature for 18 h). (f) Optical images of the 3.3Co-ZIF-8 precursors produced in a single batch with different reacting dosages. (g) The proposed formation mechanism of the hollow-structure Co-ZIF-8 precursor particles.

practical and industrially viable route for large-scale fabrication of MOF-derived Co–N–C catalysts, overcoming the solvent reliance and batch limitations of conventional wet-chemistry routes.

To understand the driving forces behind the formation of Co-ZIF-8, we conducted *ex situ* XRD analysis at different solid reaction temperatures (Fig. 1e). The results reveal that the lowest temperature for a fully developed Co-ZIF-8 structure appear at above 145 °C, slightly exceeding the melting point of 2-MIm (142 °C). This indicates that surface melting of the 2-MIm particles is a necessary condition for the solid-phase reaction to occur. Another interesting phenomenon observed is that nearly all formed Co-ZIF-8 particles exhibit distinct hollow structures, which were evolved from the original solid 2-MIm@ZnO/Co_3O_4 reactant particles (Fig. S3). The hollow structure formation of the Co-ZIF-8 particles can be understood here by the well-known Kirkendall effect, which is induced by the unequal interdiffusion between solid ZnO/Co_3O_4 nanoparticles and molten 2-MIm ligands during the reaction process. Meanwhile, one should note that the presence of free metal ions (Zn and Co ions for this work) in the reaction system is a prerequisite for their self-assembly with 2-MIm ligands to

form Co-ZIF-8 crystals. Therefore, during the solid-phase reaction, the dissolution of Zn and Co ions from the ZnO/Co_3O_4 nanoparticle surface should occur simultaneously with the interdiffusion process. Based on these analyses, we proposed the formation mechanism of the hollow-structure Co-ZIF-8 precursor particle under solid-phase conditions as illustrated by Fig. 1g.

Structure of the Co-ZIF-8-derived Co–N–C catalysts

The ball-milled *m*Co-ZIF-8 precursors were further pyrolyzed into Co–N–C catalysts (marked as *m*Co–NC-*T*, *T* denoting the pyrolysis temperature) without any post-treatments. For the 1/2/3.3Co–NC-1100 series catalysts, no diffraction signals of Co-based crystalline species can be observed in their XRD patterns (Fig. S4), implying that Co atoms are highly dispersed in these catalysts. The broadened diffraction peaks of the graphite (002) crystal plane confirm their low graphitic crystallinity, as evident from the transmission electron microscope (TEM) images (Fig. 2a and Fig. S5). While the molar fraction of Co in the precursor reaches 5% or higher, metallic Co particles began to appear, indicating that excessively doped Co tends to aggregate during the pyrolysis. Meanwhile, the diffraction peak

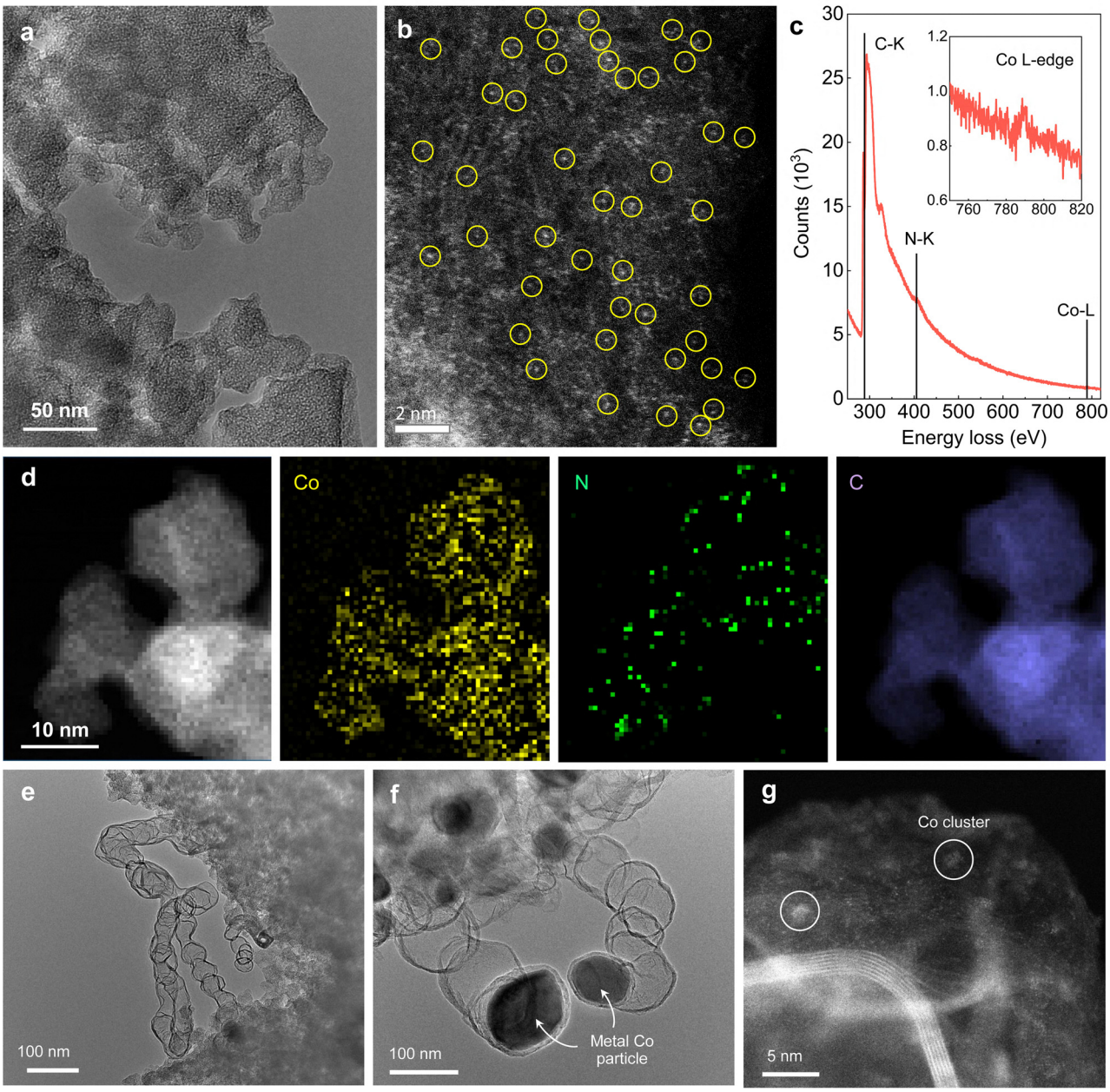

Fig. 2 Structural characterization of the synthesized Co–N–C catalysts. (a) TEM and (b) HAADF-STEM images of the 3.3Co–NC-1100 catalyst, and Co single atoms highlighted by bright yellow circles in (b). (c) STEM-EELS spectrum of the 3.3Co–NC-1100 catalyst; the inset in (c) showing the enlarged Co L-edge EELS. (d) STEM-EELS elemental mapping of the 3.3Co–NC-1100 catalyst. TEM images of the (e) 5Co–NC-1100 and (f) 10Co–NC-1100 catalysts. (g) HAADF-STEM image of the 5Co–NC-1100 catalyst.

of the graphite (002) crystal plane becomes sharper, which is ascribed to the formation of carbon nanotubes (CNTs) or hollow graphitic carbons (often encapsulating metal Co nanoparticles) as verified by both the SEM (Fig. S6) and TEM (Fig. 2e–g) results.

Notably, the Zn content in the 3.3Co–NC-1100 catalyst almost reaches zero while the Co content is ~0.94 at% as determined by the energy-dispersive X-ray spectroscopy (EDS) results (Fig. S7). The high-angle annular dark-field scanning transmission electron microscope (HAADF-STEM) image evidences the formation of single atomic Co species in the 3.3Co–NC-1100 catalyst (Fig. 2b). The distribution of Co as well as N in the carbon matrix was further evidenced by the STEM-EELS spectrum (Fig. 2c). STEM-EELS elemental mapping results (Fig. 2d) further show the uniform distribution of both N and Co on the catalyst surface, implying that the single atom Co is likely coordinated with N, thus forming the well-known Co–N_x–C_y moieties.[27]

In addition to the distribution of single atomic Co species and N, the pore structure is another key parameter for ORR electrocatalysis in PEM fuel cells. SEM images of the 3.3Co–NC-1100 catalyst (Fig. S8) exhibit the stacking of the macropores due to the aggregation of primary catalyst particles. N_2 isothermal adsorption/desorption results (Fig. S9 and Table S1) further demonstrate the presence of a large number of micropores in this catalyst, which is crucial for anchoring high-loading single-atom Co sites on the catalyst surface.

To better understand the chemical states and local coordination environments of these single Co atoms, X-ray photoelectron spectroscopy (XPS) and X-ray adsorption spectroscopy (XAS) were further conducted. High-resolution N 1s XPS spectra for all the Co–N–C catalysts (Fig. 3a and Fig. S10) were convolved into four peaks, including pyridinic N (398.5 eV), N coordinated with a single Co atom (N_x–Co, 399.5 eV), graphitic N (401.2 eV) and oxidized N (403.2 eV).[28] Semi-quantitative analysis shows that the 3.3Co–NC-1100 catalyst has the highest

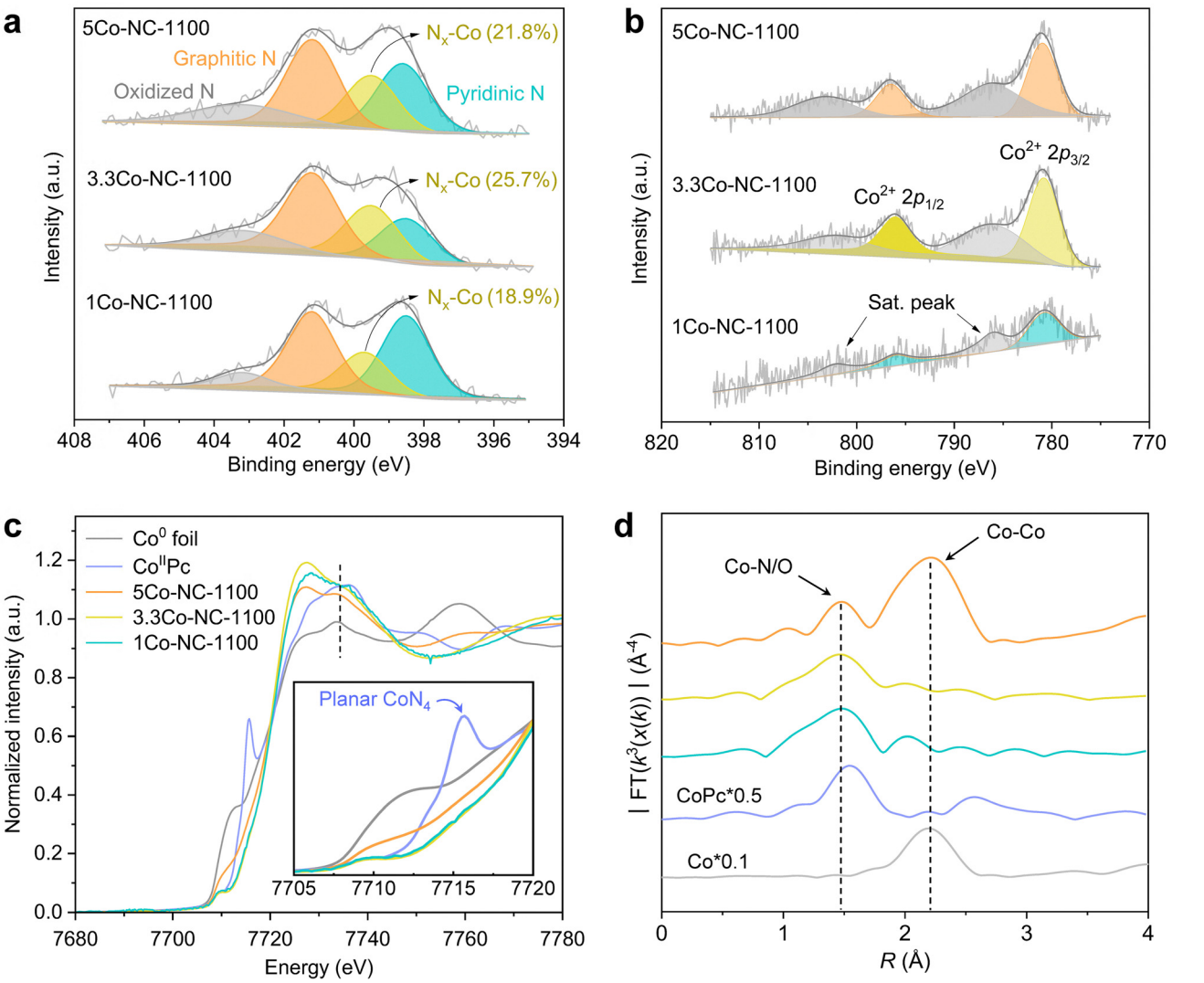

Fig. 3 Spectroscopic characterization of the Co–N–C catalysts. High-resolution (a) N 1s and (b) Co 2p XPS spectra. (c) Co K-edge XANES. (d) Co K-edge Fourier transform of k^3-weighted EXAFS spectra.

relative content of N_x–Co (25.7%) (Table S2). Co 2p XPS spectra (Fig. 3b) show only one main peak with a binding energy of 780.8 eV and 796.0 eV in the Co $2p_{3/2}$ and Co $2p_{1/2}$ regions, respectively, which can well be assigned to Co^{2+}.[29] The presence of the Co $2p_{3/2}$ satellite peak at 786.1 eV further verifies the oxidation states of the detected Co as +2.[30] Notably, no Co^0 signals were observed in the Co 2p XPS of the 5Co–NC-1100 catalyst, which seems to contradict with the XRD and SEM results. This may be ascribed to the fact that the majority of Co^0 metal nanoparticles in the 5Co–NC-1100 catalyst are encapsulated in multi-layer graphitic carbons/carbon nanotubes, whose thickness surpasses the effective detection depth of XPS. High-resolution XPS spectra of other elements (C 1s, O 1s, Zn 2p) and their semi-quantitative analysis results are given for reference in Fig. S11 and Table S3, respectively. Interestingly, as the Co-doping concentration in the Co-ZIF-8 precursor increases, the residual Zn content in the pyrolyzed catalyst shows a decreasing trend; especially when the Co concentration reaches 3.3% or higher, no XPS signal of any Zn species can be detected. This indicates that the residual Zn (mainly in the form of single-atom Zn–N_x)[5] can be replaced by Co atoms during the high-temperature pyrolysis and intend to form Co–N_x sites.[31]

Fig. 3c and Fig. S12a shows the Co K-edge X-ray absorption near edge structure (XANES) of the *m*Co–NC catalysts. The edge energies of the 1/2/3.3Co–NC-1100 catalysts ($\sim$7735 eV) closely match that of the $Co^{II}Pc$ reference sample, indicating that the oxidation state of Co in these catalysts is predominantly Co^{2+},[11] consistent with the Co 2p XPS analysis. In contrast, the Co K-edge absorption energy of the 5/10Co–NC-1100 catalysts situate between Co^0 foil and $Co^{II}Pc$, suggesting the average oxidation states of Co between 0 and +2. This can be attributed to the formation of a mixture of metallic Co and Co–N_4 moieties, as supported by the XRD, TEM, and SEM results. The Fourier transforms of the extended X-ray absorption fine structure (EXAFS) (Fig. 3d and Fig. S12b) provide further insights into the local coordination environments of Co atoms. The 1/2/3.3Co–NC-1100 catalysts exhibit only one main peak at $\sim$1.5 Å in *R* space, which is assigned to the first-shell Co–N scattering path.[27] The EXAFS fitting results (Fig. S13 and S14 and Table S4) further show that the coordination number (CN) of Co in these catalysts is around 4.0, thus strongly indicating the presence of only atomically dispersed Co atoms in the carbon matrix. In contrast, the 5/10Co–NC-1100 catalysts exhibit two main peaks: one at $\sim$1.5 Å, and another at $\sim$2.2 Å stemming from the Co–Co scattering path. This dual peak pattern verifies the coexistence of Co–N_x–C_y moieties and metallic Co in these catalysts, corroborating the structural inferences from the above analyses.

Catalytical performance evaluation of the Co–N–C catalysts

The ORR activity of the synthesized Co–N–C catalysts was first evaluated in 0.1 M $HClO_4$ electrolyte using the rotating disk electrode (RDE). The steady-state polarization plots in Fig. 4a show that the 3.3Co–NC-1100 catalyst delivers the highest ORR activity with a half-wave potential ($E_{1/2}$) of 0.782 V, which is slightly higher than that of the 1Co–NC-1100 catalyst but much higher than that of the 5Co–NC-1100 catalyst. This implies that the excessive Co doping in the precursor results in a significant decrease in the number of active sites (mainly the Co–N_4–C_y moieties), which should be caused by the formation of metal Co nanoparticles (ORR-inactive).

To elucidate the effect of the pyrolysis temperature on the ORR activity, we systematically investigated the structural evolution of Co sites during pyrolysis. The ORR activity of the 3.3Co–NC-*T* series catalysts presents a monotonically increasing trend with rising pyrolysis temperature (Fig. S15). Notably, the 3.3Co–NC-700 catalyst shows no measurable ORR current, indicating the absence of active sites at 700 °C. A sharp increase in activity is observed at 800 °C, suggesting that this is the minimum temperature required for the formation of ORR-active Co species, likely the Co–N_4–C_y moieties. Complementary XRD results (Fig. S16) confirm that the carbon framework structure in the catalyst begins to form at 800 °C, underscoring the critical role of the local coordination environment (both N and C) in governing the intrinsic ORR activity of single-atom Co sites. It is worth emphasizing again that no X-ray diffraction signals of any Co-based crystalline species can be detected for all the pyrolyzed products, further demonstrating the achievement of atomic-level Co doping in the ZIF-8 crystal structure during the solid-phase reaction.

Inductively coupled plasma optical emission spectra (ICP-OES) for these catalysts were quantitatively analyzed to interpret the observed activity evolution profiles with pyrolysis temperature. As shown in Fig. S17, a continuous increase in Co doping contents with increasing temperatures, accompanied by a progressive decrease in Zn content, suggests that pyrolysis at a higher temperature facilitates the formation of a larger number of active single-atom Co sites, thus enhancing ORR activity. The ORR selectivity was further assessed by rotating ring disk electrode (RRDE) measurements. As shown in Fig. 4b, compared to the controlled NC-1100 catalyst, the 3.3Co–NC-1100 catalyst exhibits a significantly higher four-electron selectivity with an H_2O_2 yield of less than 5% across the 0.5 V–0.7 V range. This performance is comparable to that of the commercial Pt/C catalyst, highlighting the high ORR selectivity of the Co–N_4–C_y moieties in the 3.3Co–NC-1100 catalyst.

Accelerated stress tests (ASTs) were conducted to evaluate the operation stability/durability of the 3.3Co–NC-1100 catalyst. As shown in Fig. 4c, the 3.3Co–NC-1100 catalyst exhibited excellent operation stability, as evidenced by only 11 mV loss of $E_{1/2}$ after 10 000 square cycles between 0.6 and 1.0 V *vs.* RHE in O_2-saturated 0.1 M $HClO_4$ solution. Consistent with previous studies,[32] a slight increase in double-layer capacitance was also observed for the AST-treated catalyst (inset of Fig. 4c), suggesting that carbon oxidation may occur during the stability tests. Long-term durability was then examined by holding the catalyst at 0.7 V for 100 h, after which it retained 82.5% of its initial current density (Fig. 4d), with a 39-mV loss of $E_{1/2}$ (Fig. 4e). The moderate increase in double-layer current (Fig. 4f) also supports carbon oxidation as a possible degradation mechanism

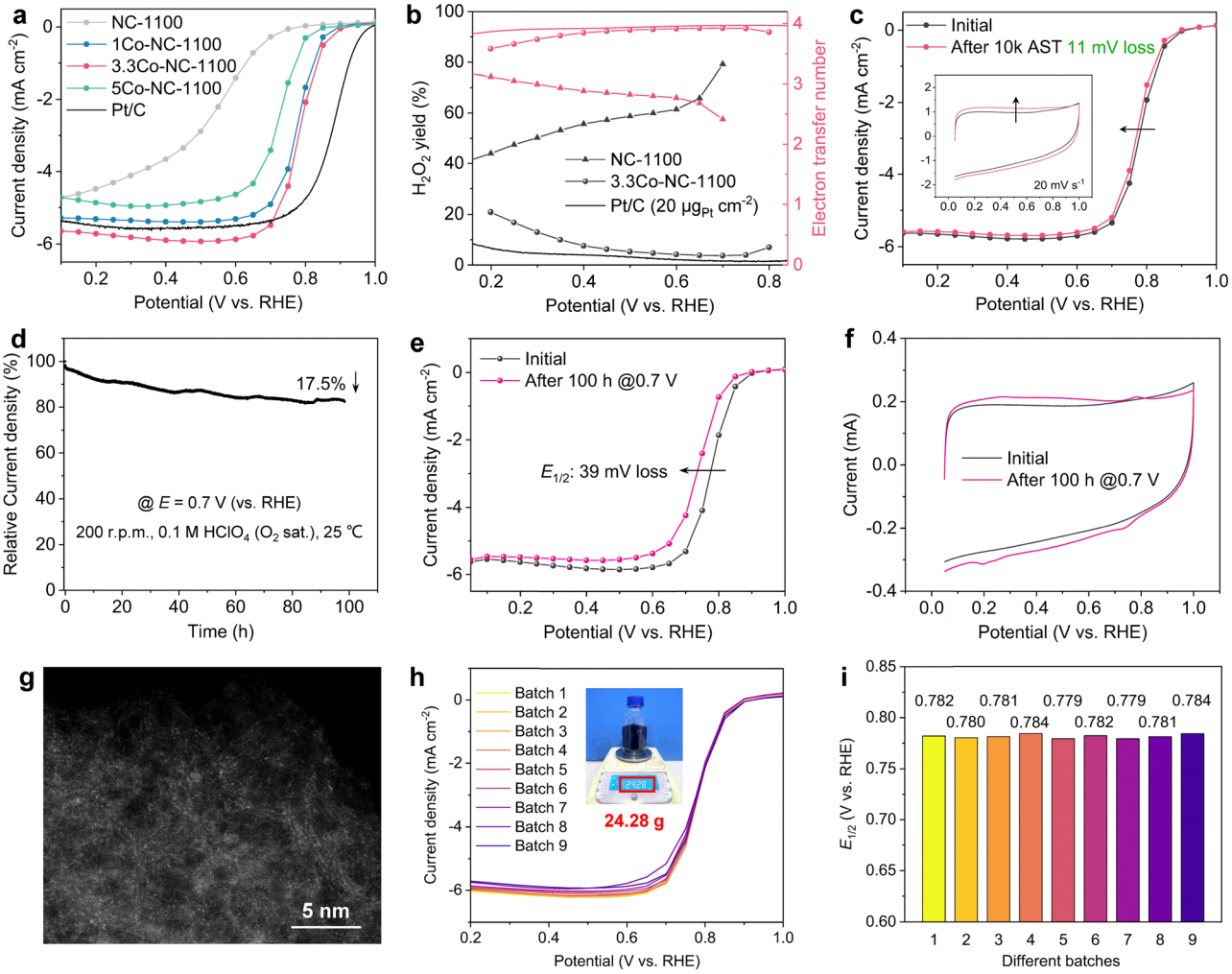

Fig. 4 Electrochemical characterization (in 0.1 M $HClO_4$ solution) of the synthesized Co–N–C catalysts. (a) Steady-state ORR polarization plots. (b) ORR selectivity (evaluated by the H_2O_2 yield and electron transform number) of the NC-1100, 3.3Co–NC-1100, and Pt/C catalysts. (c) Steady-state ORR polarization plots of the 3.3Co–NC-1100 catalyst before and after square potential cycling (O_2-saturated) between 0.6 and 1.0 V (holding 3 s at each potential). The inset shows the corresponding CV curves before and after the AST. (d) Chronoamperometric curve (@0.7 V) of the 3.3Co–NC-1100 catalyst. (e) Steady-state ORR polarization plots and (f) CV curves before and after the constant-potential test at 0.7 V for 100 h. (g) Aberration-corrected HAADF-STEM images of the 100 h AST-treated 3.3Co–NC-1100 catalyst. (h) Steady-state polarization curves of the 3.3Co–NC-1100 catalysts from 9 parallel batches, the inset showing the single-batch production (24.28 g) from 100-g 3.3Co-ZIF-8 precursors. (i) The comparison of $E_{1/2}$ values calculated from (h).

during this AST process. Notably, despite the nearly identical capacitance increase (~5%) following both AST protocols, the degree of activity decay differs significantly ($E_{1/2}$ loss: 11 mV *vs.* 39 mV). This discrepancy emphasizes that except for the carbon surface oxidation like the formation of oxygen-containing functional groups, the leaching of single atom Co sites also results in activity degradation especially under potentiostatic conditions at high operation potential. HAADF-STEM images (Fig. 4g and Fig. S18) reveal no Co oxide particles in the potentiostatic AST-treated catalyst, demonstrating that the leached Co atoms seem to diffuse into the electrolyte rather than re-depositing or aggregating into secondary phases. This is analogous to the case reported in Fe–N–C single-atom catalysts,[10] further underscoring the challenges associated with improving the intrinsic stability of Co–N_4–C_y active sites in acidic media.

Lastly, we prepared 9 parallel batches of the 3.3Co–NC-1100 catalyst (~24 g per batch, Fig. 4h inset) to evaluate the reproducibility of the solid-phase strategy proposed in this work. With the same testing conditions, the oxygen reduction polarization curves (Fig. 4h) for the different-batch catalysts were recorded. As can be seen, these curves exhibit a minimal $E_{1/2}$ variation range of only 5 mV, with the maximum at 0.784 V and the minimum at 0.779 V (Fig. 4i). This fully demonstrates the high reproducibility of the proposed strategy, representing a critical advancement for enabling the scalable application of Co–N–C single-atom catalysts.

To further evaluate the practicability of the best-performing 3.3Co–NC-1100 catalyst in PEMFCs, we tested its activity and stability performance in a single PEMFC (electrode area 4 cm^2), which was assembled with 3.3Co–NC-1100 being the cathode

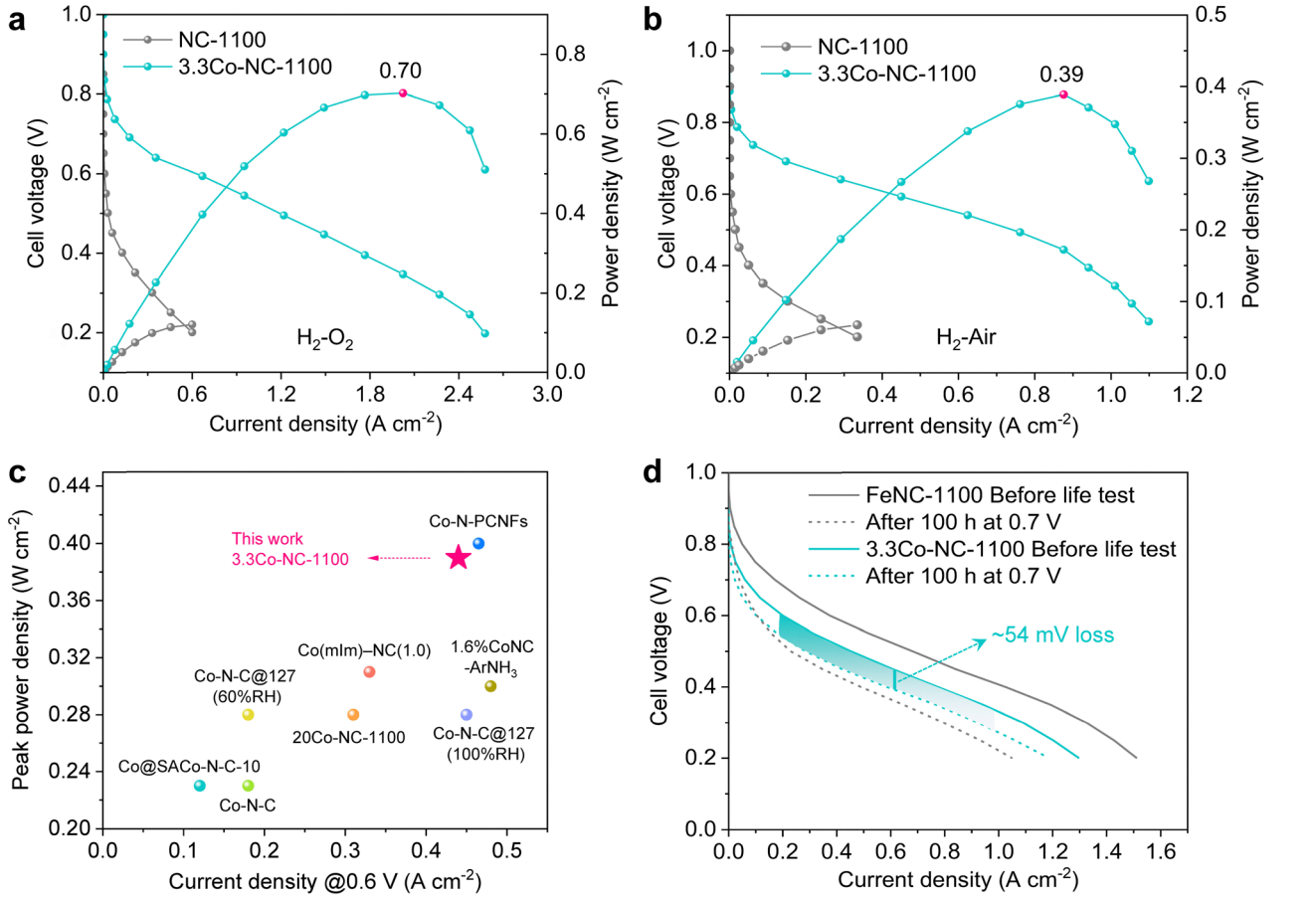

Fig. 5 PEMFC performance evaluation. (a) H_2–O_2 PEMFC polarization plots. Cathode: 3.7 mg cm^{-2}; I/C 0.67; O_2 200 sccm; 100%RH; backpressure 2.0 bar. Anode: 0.2 mg_{Pt} cm^{-2} Pt/C; I/(Pt/C) 1; H_2 200 sccm; 100%RH; backpressure 2.0 bar; membrane: Nafion 211; cell: 80 °C; 4 cm^2 electrode area. (b) H_2–air PEMFC polarization plots: cathode: air 500 sccm; other parameters are the same as the H_2–O_2 testing case. (c) H_2/air PEMFC performance comparison between 3.3Co–NC-1100 and the literature reported Co-based catalysts.[11,14,15,33–35] (d) H_2–air polarization plots before and after a 100-h life test at 0.7 V (H_2–air, backpressure 1.0 bar).

catalyst and commercial Pt/C the anode catalyst. As shown in Fig. 5a and Fig. S19, the 3.3Co–NC-1100 catalyst-assembled PEMFC exhibits respectable activity performance with a peak power density of 0.70 W cm^{-2}, which is far higher than that of the controlled NC-1100 catalyst. When the reacting gas fed into the cathode was switched to air, the peak power density can still reach up to 0.39 W cm^{-2} (Fig. 5b), which is among the best activity performances of Co-based catalysts reported in the literature (Fig. 5c). The PEMFC operation stability test for the 3.3Co–NC-1100 catalyst was conducted at a practical voltage of 0.7 V for 100 h under H_2–air conditions, and the polarization plots before and after this life test were collected. As evident in Fig. 5d, after such a relatively high voltage (*i.e.*, 0.7 V) life test, only around 54 mV voltage loss across most current density ranges was observed in the polarization plots. By contrast, the PEMFC assembled with a cathodic FeNC-1100 single-atom catalyst (prepared by the solid-phase method proposed in this work, Fig. S20 presenting its microstructural characterizations) showed an average voltage loss of 170 mV after the same AST. This result again consolidates the stability advantage of Co–N–C single-atom catalysts over Fe–N–C.[3,11]

Conclusion

In summary, we have reported a solid-phase strategy for large-scale production of Co-ZIF-8-derived Co–N–C single-atom electrocatalysts, overcoming the scalability and environmental limitations of conventional wet-chemistry methods. By directly driving the reaction of the solid 2-MIm@ZnO/Co_3O_4 mixture, we synthesized kilogram-scale Co-doped ZIF-8 precursors *via* the Kirkendall effect while achieving precise compositional control (0–80% Co incorporation). Employing HAADF-STEM, XPS, and XAS analyses, we establish that the final Co–N–C catalyst structure strongly depends on the precursor composition—where excessive Co loading leads to metallic Co particle formation, while optimized doping yields atomically dispersed $Co–N_4$ active sites. We demonstrate that the optimized Co–N–C catalyst achieves high ORR activity ($E_{1/2}$ = 0.782 V), excellent four-electron selectivity (H_2O_2 yield <5%), and long-term stability. When integrated into a PEMFC cathode, our catalyst delivers respectable power densities of 0.70 W cm^{-2} and 0.39 W cm^{-2} under H_2–O_2 and H_2–air, respectively, both of which are ranked among the best Co-based catalysts reported. The superior PEMFC operation stability of our Co–N–C catalyst

to that of Fe–N–C was also well demonstrated. Through this work, we establish a scalable, environmentally friendly approach for producing high-performance Co–N–C single-atom electrocatalysts and we expect this strategy to accelerate the practical deployment of TM–N–C catalysts in next-generation fuel cells and beyond.

Conflicts of interest

There are no conflicts to declare.

Data availability

The data supporting this article have been included as part of the supplementary information (SI). Supplementary information is available. See DOI: **https://doi.org/10.1039/d5ey00264h**.

Acknowledgements

We gratefully acknowledge the support from Guangdong Basic and Applied Basic Research Foundation (2023A1515140002), National Natural Science Foundation of China (52173222), and Shenzhen Science and Technology Innovation Committee (ZDSYS20230626091100001, JCYJ20230807111605012). We acknowledge DESY (Hamburg, Germany), a member of the Helmholtz Association HGF, for the provision of experimental facilities. Parts of this research was carried out at PETRA III and we would like to thank Wolfgang Caliebe for assistance in using the P64 beamline. Beamtime was allocated for proposal I-20240509 EC. We would like to express our gratitude to Dr Michael Haumann and Prof. Holger Dau from Freie Universität Berlin for providing access to the SimXLite software (for EXAFS fit) developed by the scientists at the KMC-3 beamline at BESSY-HZB.

References

1 J. Fan, M. Chen, Z. Zhao, Z. Zhang, S. Ye, S. Xu, H. Wang and H. Li, *Nat. Energy*, 2021, **6**, 475–486.
2 J. Bai, Y. Lin, J. Xu, W. Zhou, P. Zhou, Y. Deng and Y. Lian, *Chem. Commun.*, 2024, **60**, 7113–7123.
3 S.-H. Yin, S.-L. Yang, G. Li, G. Li, B.-W. Zhang, C.-T. Wang, M.-S. Chen, H.-G. Liao, J. Yang, Y.-X. Jiang and S.-G. Sun, *Energy Environ. Sci.*, 2022, **15**, 3033–3040.
4 A. Mehmood, M. Gong, F. Jaouen, A. Roy, A. Zitolo, A. Khan, M.-T. Sougrati, M. Primbs, A. M. Bonastre, D. Fongalland, G. Drazic, P. Strasser and A. Kucernak, *Nat. Catal.*, 2022, **5**, 311–323.
5 L. Jiao, J. Li, L. L. Richard, Q. Sun, T. Stracensky, E. Liu, M. T. Sougrati, Z. Zhao, F. Yang, S. Zhong, H. Xu, S. Mukerjee, Y. Huang, D. A. Cullen, J. H. Park, M. Ferrandon, D. J. Myers, F. Jaouen and Q. Jia, *Nat. Mater.*, 2021, **20**, 1385–1391.
6 X. Wan, X. Liu, Y. Li, R. Yu, L. Zheng, W. Yan, H. Wang, M. Xu and J. Shui, *Nat. Catal.*, 2019, **2**, 259–268.
7 Y. Li, P. Zhang, L. Wan, Y. Zheng, X. Qu, H. Zhang, Y. Wang, K. Zaghib, J. Yuan, S. Sun, Y. Wang, Z. Zhou and S. Sun, *Adv. Funct. Mater.*, 2021, **31**, 2009645.
8 Y. Chu, Y. Cheng, P. Wang, J. Bai, X. Guan, S. Wang, C. Lan, H. Wu, Z. Shi, S. Zhu, W. Liu, C. Liu, M. Xiao and W. Xing, *Sci. China: Chem.*, 2024, **68**, 1541–1549.
9 H. Xie, X. Xie, G. Hu, V. Prabhakaran, S. Saha, L. Gonzalez-Lopez, A. H. Phakatkar, M. Hong, M. Wu and R. Shahbazian-Yassar, *Nat. Energy*, 2022, **7**, 281–289.
10 K. Kumar, L. Dubau, M. Mermoux, J. Li, A. Zitolo, J. Nelayah, F. Jaouen and F. Maillard, *Angew. Chem., Int. Ed.*, 2020, **59**, 3235–3243.
11 X. Xie, C. He, B. Li, Y. He, D. A. Cullen, E. C. Wegener, A. J. Kropf, U. Martinez, Y. Cheng, M. H. Engelhard, M. E. Bowden, M. Song, T. Lemmon, X. S. Li, Z. Nie, J. Liu, D. J. Myers, P. Zelenay, G. Wang, G. Wu, V. Ramani and Y. Shao, *Nat. Catal.*, 2020, **3**, 1044–1054.
12 D. Banham, S. Ye, K. Pei, J.-i Ozaki, T. Kishimoto and Y. Imashiro, *J. Power Sources*, 2015, **285**, 334–348.
13 K. Liu, S. Kattel, V. Mao and G. Wang, *J. Phys. Chem. C*, 2016, **120**, 1586–1596.
14 Y. He, S. Hwang, D. A. Cullen, M. A. Uddin, L. Langhorst, B. Li, S. Karakalos, A. J. Kropf, E. C. Wegener, J. Sokolowski, M. Chen, D. Myers, D. Su, K. L. More, G. Wang, S. Litster and G. Wu, *Energy Environ. Sci.*, 2019, **12**, 250–260.
15 X. X. Wang, D. A. Cullen, Y.-T. Pan, S. Hwang, M. Wang, Z. Feng, J. Wang, M. H. Engelhard, H. Zhang, Y. He, Y. Shao, D. Su, K. L. More, J. S. Spendelow and G. Wu, *Adv. Mater.*, 2018, **30**, 1706758.
16 P. Yin, T. Yao, Y. Wu, L. Zheng, Y. Lin, W. Liu, H. Ju, J. Zhu, X. Hong, Z. Deng, G. Zhou, S. Wei and Y. Li, *Angew. Chem., Int. Ed.*, 2016, **55**, 10800–10805.
17 M. Chen, X. Li, F. Yang, B. Li, T. Stracensky, S. Karakalos, S. Mukerjee, Q. Jia, D. Su, G. Wang, G. Wu and H. Xu, *ACS Catal.*, 2020, **10**, 10523–10534.
18 J. Li, M. Chen, D. A. Cullen, S. Hwang, M. Wang, B. Li, K. Liu, S. Karakalos, M. Lucero, H. Zhang, C. Lei, H. Xu, G. E. Sterbinsky, Z. Feng, D. Su, K. L. More, G. Wang, Z. Wang and G. Wu, *Nat. Catal.*, 2018, **1**, 935–945.
19 H. Zhang, S. Hwang, M. Wang, Z. Feng, S. Karakalos, L. Luo, Z. Qiao, X. Xie, C. Wang, D. Su, Y. Shao and G. Wu, *J. Am. Chem. Soc.*, 2017, **139**, 14143–14149.
20 Y. Chen, S. Ji, Y. Wang, J. Dong, W. Chen, Z. Li, R. Shen, L. Zheng, Z. Zhuang, D. Wang and Y. Li, *Angew. Chem., Int. Ed.*, 2017, **56**, 6937–6941.
21 S. Ma, G. A. Goenaga, A. V. Call and D. J. Liu, *Chem. - Eur. J.*, 2011, **17**, 2063–2067.
22 M. Xiao, H. Zhang, Y. Chen, J. Zhu, L. Gao, Z. Jin, J. Ge, Z. Jiang, S. Chen, C. Liu and W. Xing, *Nano Energy*, 2018, **46**, 396–403.
23 J.-B. Lin, R.-B. Lin, X.-N. Cheng, J.-P. Zhang and X.-M. Chen, *Chem. Commun.*, 2011, **47**, 9185–9187.
24 D. Zhao, J.-L. Shui, L. R. Grabstanowicz, C. Chen, S. M. Commet, T. Xu, J. Lu and D.-J. Liu, *Adv. Mater.*, 2014, **26**, 1093–1097.
25 Q. Liu, X. Liu, L. Zheng and J. Shui, *Angew. Chem., Int. Ed.*, 2018, **57**, 1204–1208.

26 A. Uddin, L. Dunsmore, H. Zhang, L. Hu, G. Wu and S. Litster, *ACS Appl. Mater. Interfaces*, 2020, **12**, 2216–2224.
27 W. Xu, R. Zeng, M. Rebarchik, A. Posada-Borbón, H. Li, C. J. Pollock, M. Mavrikakis and H. D. Abruña, *J. Am. Chem. Soc.*, 2024, **146**, 2593–2603.
28 K. Artyushkova, *J. Vac. Sci. Technol., A*, 2020, **38**, 031002.
29 H. Zou, W. Rong, S. Wei, Y. Ji and L. Duan, *Proc. Natl. Acad. Sci. U. S. A.*, 2020, **117**, 29462–29468.
30 D. Singh, I. I. Soykal, J. Tian, D. von Deak, J. King, J. T. Miller and U. S. Ozkan, *J. Catal.*, 2013, **304**, 100–111.
31 R. Kumar, M. Mooste, Z. Ahmed, S. Akula, I. Zekker, M. Marandi, M. Käärik, J. Leis, A. Kikas, A. Treshchalov, M. Otsus, J. Aruväli, V. Kisand, A. Tamm and K. Tammeveski, *Ind. Chem. Mater.*, 2023, **1**, 526–541.
32 D. Xia, C. Yu, Y. Zhao, Y. Wei, H. Wu, Y. Kang, J. Li, L. Gan and F. Kang, *Chem. Sci.*, 2021, **12**, 11576–11584.
33 Q. Cheng, S. Han, K. Mao, C. Chen, L. Yang, Z. Zou, M. Gu, Z. Hu and H. Yang, *Nano Energy*, 2018, **52**, 485–493.
34 Y. He, H. Guo, S. Hwang, X. Yang, Z. He, J. Braaten, S. Karakalos, W. Shan, M. Wang, H. Zhou, Z. Feng, K. L. More, G. Wang, D. Su, D. A. Cullen, L. Fei, S. Litster and G. Wu, *Adv. Mater.*, 2020, **32**, e2003577.
35 L. Chen, X. Liu, L. Zheng, Y. Li, X. Guo, X. Wan, Q. Liu, J. Shang and J. Shui, *Appl. Catal., B*, 2019, **256**, 117849.